Medical Engineering and Physics 69 (2019) 58–71

Contents lists available at ScienceDirect

Medical Engineering and Physics

journal homepage: www.elsevier.com/locate/medengphy

Image-based anatomical reconstruction and pharmaco-mediated bone remodeling model applied to a femur with subtrochanteric fracture: A subject-specific finite element study

Miguel T. Bahia[a,b,*], Mildred B. Hecke[b], Emílio G.F. Mercuri[b,c]

[a] Departamento de Mecânica, Instituto Federal de Santa Catarina - Campus Joinville, Joinville, SC, Brazil
[b] Grupo de Bioengenharia, Programa de Pós-Graduação em Métodos Numéricos em Engenharia, Universidade Federal do Paraná, Curitiba, Brazil
[c] Departamento de Engenharia Ambiental, Universidade Federal do Paraná, Curitiba, Brazil

ARTICLE INFO

Article history:
Received 4 July 2018
Revised 17 April 2019
Accepted 19 May 2019

Keywords:
Subject-specific finite element modeling
Computed tomography (CT)
Image processing
Bone biomechanics
Young's modulus
Femur
Mathematical modeling

ABSTRACT

Patient-specific finite element (FE) models are constructed in a way that boundary conditions, material and geometric FE models respect the unique characteristics of the patients, offering a more reliable and realistic structural analysis. This study presents an image-based construction process of a patient-specific FE model applied to a femur with a subtrochanteric fracture. Available procedures are systematized and described in greater depth aiming to investigate the difficulties and possibilities in the development of this type of model. A set of image processing techniques (segmentation, labeling, morphological operations and registering) were performed for volumetric reconstruction and registration of femoral fragments by assessing computed tomography (CT) images in a semi supervised procedure. The CT numbers feed the FE mesh with a non-homogeneous distribution of elasticity modulus. A FE analysis and a bone remodeling simulation with pharmacological stimulus based on the dynamics of bone cells populations were also developed for this study. The FE analysis revealed that the principal stresses provided results close to those obtained using a generic homogeneous model, with a difference of about 2%. In contrast, principal strains presented significant differences, up to 12 and 21 % for the maximum tensile and compressive principal strain values, respectively. The critical values of tensile principal strains were located in the superior part of the femoral neck, a typical region of femoral fractures, and maximum principal strains 2 and 3 (compressive) were concentrated in the diaphyseal region, rather close to the actual fracture. These results corroborate previous works indicating that the strain-based failure criterion is more successful in capturing the bone fracture sites when compared to stress-based criteria. The attempt to reconstruct the material state before the failure as implemented here constitutes an innovative way to analyze and reconstruct bone fractures. In the bone remodeling simulation, the inclusion of an antiresorptive agent stimulus produced cortical bone thickening, an increase in the BMD biomarker, and an overall increase in the bone ash density, just as expected in an osteoporosis therapeutic treatment. In conclusion, this study highlights the advantages of subject-specific FE models compared to generic ones in the study of abnormal clinical cases, evaluation of fracture risk, and optimization of surgical intervention. On the other hand, the high level of human intervention and expertise involved in patient-specific FE analyses hinders the incorporation of this technique into clinical practice.

1. Introduction

Bone diseases have a major impact on the quality of life of men and women, particularly after the age of 50. Osteoporosis, characterized by an imbalance in the natural bone remodeling process, results in lower bone quality, as a consequence, greater exposure to the risk of fractures. Elderly patients with femoral fractures live less and are more likely to become dependent or institutionalized [1,2]. It is estimated that the mortality rate among patients with osteoporotic fractures reaches 15–30% due to complications associated with the disease itself such as infections, venous thrombosis and cardiovascular diseases [3].

Structural analysis of the bone using the finite element method (FEM) usually adopts homogeneous isotropic material with

---

[*] Corresponding author at: Departamento de Mecânica, Instituto Federal de Santa Catarina, Rua Pavão, 1377, Costa e Silva, CEP 89220-618 Joinville, Santa Catarina, Brazil.

E-mail addresses: migueltbahia@ifsc.edu.br, migueltbahia@gmail.com (M.T. Bahia).

https://doi.org/10.1016/j.medengphy.2019.05.005
1350-4533/

constant Young modulus and constant Poisson ratio for cortical and trabecular bone [4–6], which is a pragmatic but unrealistic approach. Bone exhibits non-homogeneous material properties, anisotropic behavior and a dependence of tissue density on age and mineralization level [7]. The material characterization should be able to capture the heterogeneous physical properties according to bone site [8] and according to individual characteristics such as age and gender [9]. When using finite element (FE) analyses to study special clinical cases, in which the risk of fracture must be evaluated, the stress and strain states can be more reliably and accurately assessed if they are based on specific patient properties [5,10–13]. Medical images, originated from CT, MRI and others scans, reveals material properties and patient specific geometric features, making it an essential tool for the construction of this kind of model.

Various aspects impact the accuracy of the final subject-specific FE model [14]: image acquisition parameters [15,16]; segmentation technique [17,18], FE mesh generation, assignment of material properties and boundary conditions. Image quality and resolution depend greatly on the characteristics of the acquisition device and the parameters adopted for the scan [19]. The fusion of adjacent parts of bones is usually observed in low resolution images [17]. Distorted and low contrast on edges due to osteoporosis, passage of blood vessels or overlapping of pixels values make simple histogram-based segmentation methods inappropriate [18]. Combination of different segmentation techniques are frequently used to overcome the limitations of individual methods. These combination include:*edge-based* algorithms, which are based on gradient fields; *region-based* algorithms, that group regions that meet certain homogeneity criteria; *deformable algorithms*, that morph a priori shape into image data; and finally the *active contouring* [14,20]. Regarding mesh discretization (third aspect), highly distorted mesh elements or even a very coarse mesh in regions subjected to high stresses may result in well-deteriorated numerical solutions. Criteria to assess mesh quality and suitability should be implemented to characterize the accuracy of the FE solution. Some error estimators are available in finite element packages to this end. These are obstacles that must be circumvented for the automation of individualized FE models. Automation is one of the fundamental conditions to consolidate the method as a routine clinical tool [12].

In this perspective, the present work aims to investigate the use of CT scans to build an accurate subject-specific FE model, systematizing and describing in greater depth some techniques commonly adopted. The limitations imposed by the low resolution of the medical images used in this study forced us to pursue different strategies to overcome the difficulties typically found when building this kind of FE model. Here, we develop an image-based procedure for the volumetric reconstruction and mapping of local densities of a fractured femur and apply to CT scans. We also propose a new bone remodeling model based on the dynamics of bone cells populations including mechanical and pharmacological stimulus implemented in the FE model. The core of the model is built upon the work of Lemaire et al. [21] incorporating a mechanical stimulus based on strain energy density [22] and an original regulatory function regarding drug concentration on bone sites.

The case under study here is a femur fractured in the subtrochanteric region. The most common femoral fractures occur in the femoral neck and the intertrochanteric region located between the greater and small trochanter, mainly affecting people over 50 years of age due to trauma or osteoporosis [23]. Fractures in the subtrochanteric and diaphyseal regions are uncommon and usually occur in young or middle-aged adults as a result of a high energy trauma [24,25]. Therefore, the present research also addresses a relevant case study in the field of bone diseases.

2. Materials and methods

This work investigates the use of image processing techniques in order to build a more accurate subject-specific FE model. A set of CT scans is adopted to drive and feed the process of building both geometric and material FE models. The images chosen correspond to a proximal femur with a fracture at the subtrochanteric region with lateral displacement, angularity and no continuity between fragments.

2.1. Image-based anatomical reconstruction

The 8 bits images set is composed of 243 images with 1.0 mm slice thickness, 0.391 mm pixel pitch, which corresponds to up to 3/4 of the human femur. Computer codes were written in MatLab 7.12 (R2011a) software (MathWorks, Natick, Massachusetts, US) and run in a standard personal computer (Intel Core i7 5500U CPU 2.4 GHz).

A flowchart and an overview of the procedures developed are illustrated in Figure 1. Computational implementation resulted in a 3D femur without fracture, followed by a FE analysis and a drug-driven bone cells remodeling simulation. The sequence of procedures can be enumerated as follows:

1. Conversion of 2D images into a 3D volumetric image matrix: the set of CT images are stacked at evenly spaced heights forming an 3D array of size $p_x \times p_y \times slices$, where p_x and p_y are the number of pixels of images in the x and y-axes, respectively, and *slices* refers to the number of slices or CT images, in our case, with $512 \times 512 \times 243$. The authors used 8-bits medical images with gray-level within the range of [0,255], which required the adoption of some strategies to overcome the low image quality limitations.
2. Matrix Segmentation: a two-step segmentation was necessary to handle the low resolution of images and low densities regions. K-means clustering algorithm was applied for each 2D image as an initial segmentation prior to the application of the Iterative Conditional Modes (ICM) algorithm on the 3D images [20]. Furthermore, in order to obtain a smoother contour of the femur boundaries, a sequence of morphological operations [26] such as dilation, erosion, blurring and re-thresholding was applied to each 2-D slice, as can be seen in Figure 2.
3. Labeling of connected components: after bone segmentation, each femoral fragment is labeled to allow fragments alignment and registering. The built-in Matlab function '*bwlabeln*' was used to detect regions of voxels that are contiguous to each other [27]. The labeling algorithm scans all image and groups the pixels into components based on pixel connectivity with similar pixel intensity values [28,29].
4. Registration: the identification of bone fragments is followed by sequences of affine transformations (translation, rigid body rotation and scaling) applied to the 3D point cloud data corresponding to each fragment to register the two parts of the femur in order to reconstitute its original non-fractured anatomy.
5. Generation of a surface data file (format STL): the point cloud data is imported to Meshlab [30], that compute normals for the boundaries of dataset and builds a surface using the Poisson Surface Reconstruction approach [31].
6. FE mesh: using Matlab built-in functions for mesh generation, the surface data file is converted into a solid and discretized into linear tetrahedral elements.
7. Mapping of material properties: CT numbers are translated into ash densities and mapped onto the FE mesh for the distribution of Young moduli, using an experimental relation. The algorithm evaluates whether a pixel is inside or outside the convex hull defined by the vertices of each tetrahedral finite element, and

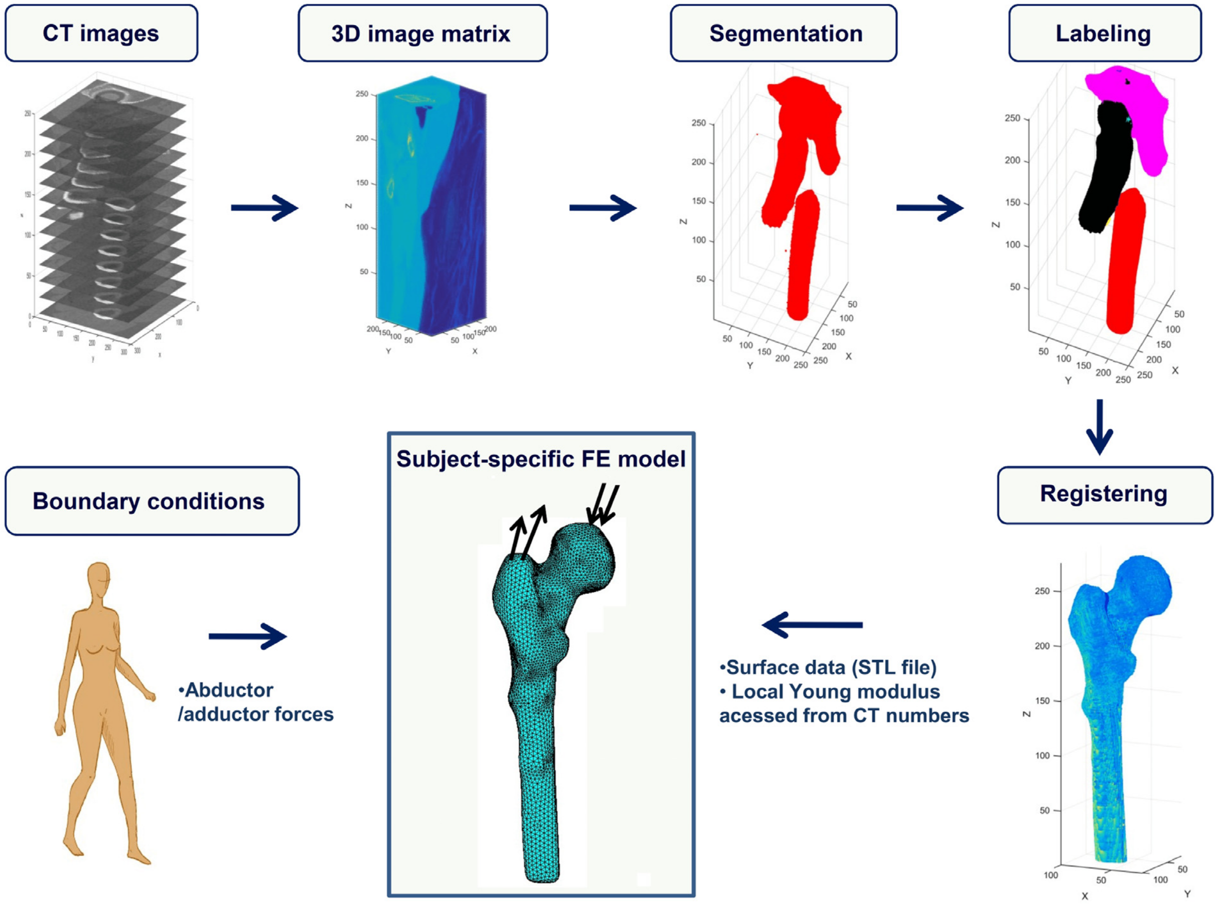

Fig. 1. Sequence employed to build the subject-specific FE model. At first, CT images are stacked forming a 3D image matrix; then, images are segmented to extract the femur; all connected components are labeled to identify the bone fragments, and registered. The second stage consists of the FE discretization process, mapping of material properties and definition of boundary conditions.

assign the average pixel value within the convex hull to each corresponding finite element adopting the strategy proposed by Zannoni et al. [32].

8. FE analysis: two different FE analysis were performed with different load cases. First, a structural static analysis was conducted with one load case applied. Then, a bone remodeling simulation using a model based on the dynamics of bone cells populations was performed with three load cases.
9. Post-processing: visualization of the results were performed using Paraview 5.0 software and Matlab scripts. The input file format adopted for Paraview was the Visualization Toolkit (VTK) [33].

2.2. Finite element model

In order to apply the proposed procedure, a FE model was built from CT images of a femur, as shown in Figure 5. The reconstructed femur was discretized in a finite element mesh with 13,114 nodes and 61,372 tetrahedral elements. The initial densities were obtained from the CT images and transferred to the FE model. The authors have adopted a linear relationship between the grayscale of pixels [0, 255] and the bone densities. The whitest pixel in the image (full bone with no voids) in the cortical bone was assigned the value of 1.4 g/cm^3, corresponding to the maximum value for bone ash density, that is the bone ash mass divided by the total volume. The darkest pixel surrounding the bone (corresponding to water) was assigned zero ash density. This strategy was necessary given the lack of scanning phantom data to convert HU to equivalent K_2HPO_4 density, which is commonly assumed to be equal to bone ash density [34]. Thus, these two extreme values define a linear interpolation which can be expressed as:

$$\rho_{\mathrm{ash}} = [p(x, y, z) - a]\frac{1.4}{b - a} \qquad [\mathrm{g/cm^3}] \tag{1}$$

where $p(x, y, z)$ is the pixel grayscale value at position (x, y, z), a and b are the image grayscale limit values for water and bone without voids, respectively. Here, the values $a = 66$ and $b = 219$ were chosen according to the image quality.

The literature describes several relationships between Young's modulus and bone densities [8,35–39]. The elasticity modulus was defined as a function of the ash densities assessed from CT images using the relation proposed by Keller [38] and validated by Yosibash et al. [40] and Trabelsi et al. [13]:

$$E_{\mathrm{cort}} = 10200\rho_{\mathrm{ash}}^{2.01} \quad [\mathrm{MPa}] \tag{2}$$

$$E_{\mathrm{trab}} = 5307\rho_{\mathrm{ash}} + 469 \quad [\mathrm{MPa}] \tag{3}$$

Trabecular and cortical bone types are distinguished with the condition $\rho_{\mathrm{ash}} > 0.6$ g/cm^3 for cortical bone and $\rho_{\mathrm{ash}} \leq 0.6$ g/cm^3 for trabecular bone [5]. Poisson's ratio was set equal to 0.3 [4,5]. The implementation of this mapping procedure resulted in an elastic modulus range of 1.06–19.46 GPa.

The histogram for pixel intensities of the 3-D image of the segmented femur is shown in Figure 3. The two bell-shaped curve

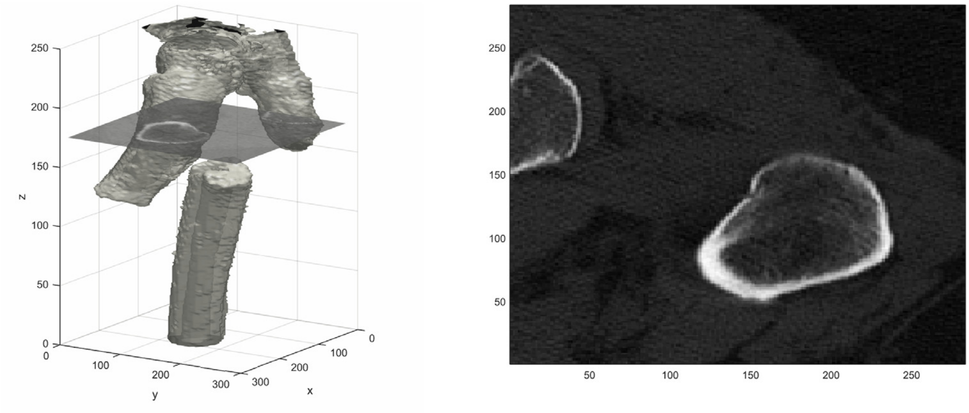

(a) Isosurface of femur

(b) Original CT image selected

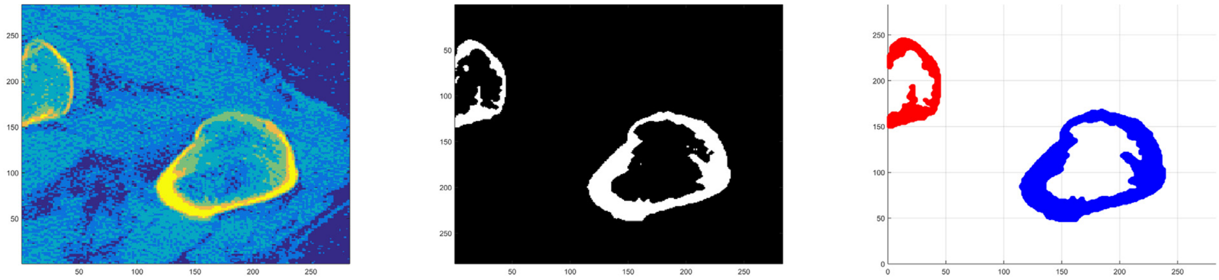

(c) k-means clustering

(d) Morphological image processing

(e) Label of connected components

Fig. 2. Basic procedures applied to each CT slice image. Morphological operations of dilatation, erosion, blurring and re-thresholding were also developed to smooth the boundaries of femur fragments, using built-in Matlab functions from the Image Processing Toolbox.

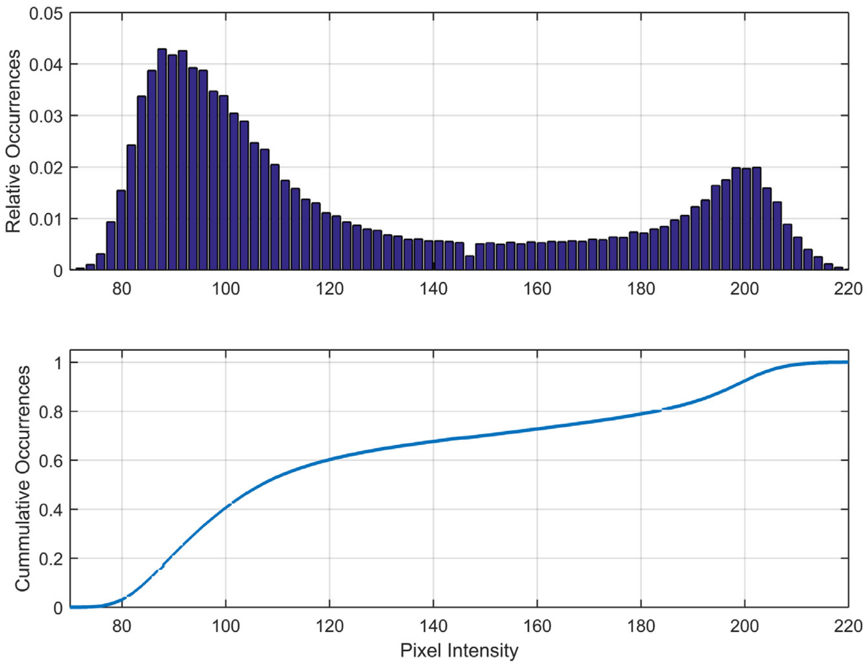

Fig. 3. Histogram and cumulative frequency of the 3-D image of the femur. Bimodal shape reveals cortical and trabecular bone types.

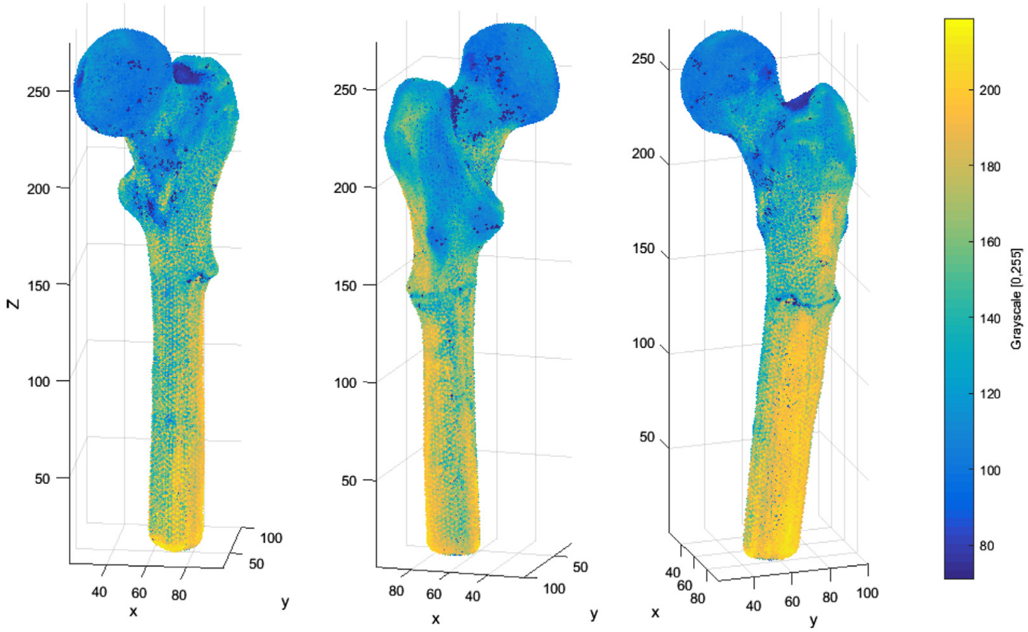

Fig. 4. Densities assessed from CT images and exported to the FE mesh. Different views of the femur mesh with grayscale values.

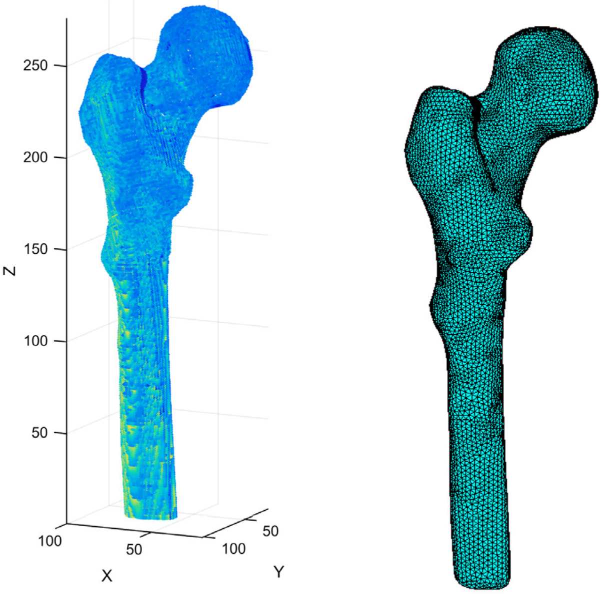

(a) Reconstructed femur.

(b) Femur mesh.

Fig. 5. Discretization of the reconstructed femur in a finite element mesh with 13,114 nodes and 61,372 tetrahedral elements (a) and assignment to gray values in mesh elements (b).

(bimodal distribution) reflects the presence of cortical and trabecular bone. Intermediate gray scale values between the two bells indicate that the bone lies in the transition limits of the two bone types. A Gaussian mixture model distribution was used to cluster the data and find the two average pixel intensities for each bone type. Figure 4 presents the result of the mapping procedure and grayscale values assigned to the finite element mesh. Thus this procedure allows the assignment of an average material property to each finite element based on density information extracted from the CT database.

In the first FE simulation (static structural analysis) the authors adopted one load case referred to one leg stance associated with a standing person. The models adopted by Nedoma et al. [41] were adapted to define the values for adductor force applied to the acetabulus and the abductor force action on the great trochanter. Considering a body weight of 680 N, a force balance provides the adductor and abductor forces, that are 2168 N and 1632 N, respectively. For the force balance acting on the pelvis, we consider that a resultant force acting on the femoral head form 16° with the z-axis and a resulting abductor force acting on the great trochanter form 22° with the z-axis [41,42]. In order to obtain a more realistic distribution, these resultant forces were proportionally distributed on the faces of finite elements in the boundaries of the femur head and greater trochanter within a specified distance, as shown in Figure 6. Furthermore, the authors assumed a proportionality between the normal to the element face and the resultant force to obtain each applied force. Such strategies aim to provide a loading case more suitable to the 3D FE simulation. The nodes of the femur's lower part were held fixed. This boundary condition does not produce the best physiological representation of the deformation pattern of the femur [43]. It was adopted here because the available CT dataset did not contain the lower extremity of the femur (or distal extremity).

Three loading cases were adopted for the bone remodeling dynamic simulation. At each iteration of the bone remodeling algorithm, the densities distribution in the cortical and trabecular bone change, requiring a configuration of forces closer to the physiological loading conditions to obtain more realistic results.

The boundary conditions of the bone remodeling simulation were based on the proposal of Carter et al. [45], which represents the joint reactions and abductor muscular forces for a standard gait cycle. For each cycle of FE analysis, three loading cases corresponding to the maximal adduction limits, maximal abduction and average support of the gait cycle were analyzed sequentially (Fig. 7). The orientations and magnitudes of the forces were adapted from Hambli et al. [44] and are listed in Table 1. The concentrated loads were transformed into equivalent proportionally distributed loads on the femoral head and greater trochanter considering that the application of forces is distributed on an area of the femoral head and the greater trochanter surfaces.

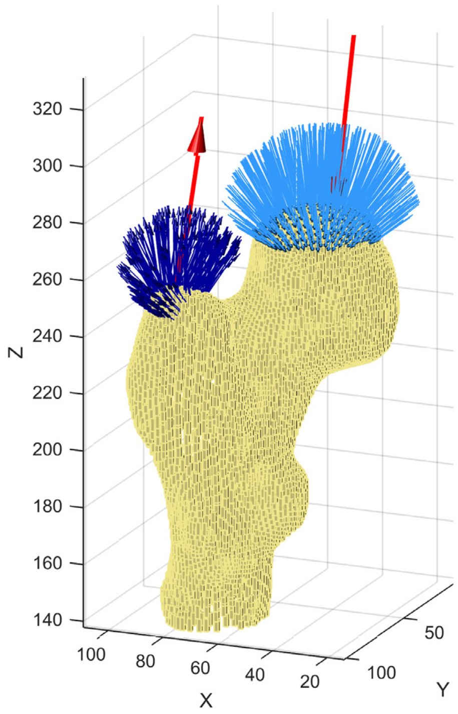

Fig. 6. Detail of the loading applied to the femur, joint forces distributed on the acetabulus and adductor forces distributed on the greater trochanter. Visualization developed in Matlab.

Table 1
Load cases used in the FE model referring to a standard gait. Orientation angles to the frontal and sagital planes [44,45].

Load	Joint Forces [N]	Orientation [deg.]		Abductors Forces [N]	Orientation [deg.]	
		Frontal	Sagittal		Frontal	Sagittal
Case 1	2317	24	6	703	28	15
Case 2	1158	−15	35	351	−8	9
Case 3	1548	56	−20	468	35	16

2.3. Cells populations model

The bone remodeling is a mechanism involving sequential osteoclast-mediated bone resorption and osteoblast-mediated bone formation at the same location, in order to promote the replacement of the bone matrix and repair of small defects (e.g., microdamage), thereby renewing the skeleton over time [46]. Lemaire et al. [21] proposes a mathematical model to describe the dynamics of bone cells populations (pre-osteoblasts, active osteoblasts and active osteoclasts) during the bone remodeling. The model includes the osteoblast-osteoclast coupling, RANK-RANKL-OPG signaling, allows the simulation of some bone metabolic diseases and also the antagonistic effects of PTH administration. The system RANK-RANKL-OPG is an important regulator of osteoclastogenesis. Disorders in this system have implications on bone remodeling and are associated with bone diseases. The interaction between RANKL (rank ligand) and its RANK receptor found in precursor osteoclasts would be controlled by osteoprotegerin (OPG), a cytosine secreted by osteoblasts, with affinity to RANKL that inhibit RANK-RANKL binding.

The Lemaire's model [21] considers four stages in the development of osteoblasts: precursors, responsive, active and a fourth group that aggregates apoptotic cells and osteocytes. In the case of non-committed precursors, they form a reservoir with a constant number of cells that can be differentiated into osteoblasts as a response to a stimulatory factor such as the TGF-β protein. This protein also acts on the responsible osteoblasts preventing their differentiation. Active osteoblasts are influenced by PTH in the control of OPG and RANKL production [47].

RANKL induces the differentiation of active osteoclasts, which release TGF-β causing osteoclastic apoptosis and control osteoblast differentiation. A graphical schematics of the model is presented in Figure 8.

The behavior of bone cells is regulated by their own cytosines or by cytosines produced by different cells. The kinetics of reactions can be represented by the law of mass action. It is worth mentioning that the original model proposed by Lemaire et al. [21], does not include the contribution of mechanical stimuli nor the

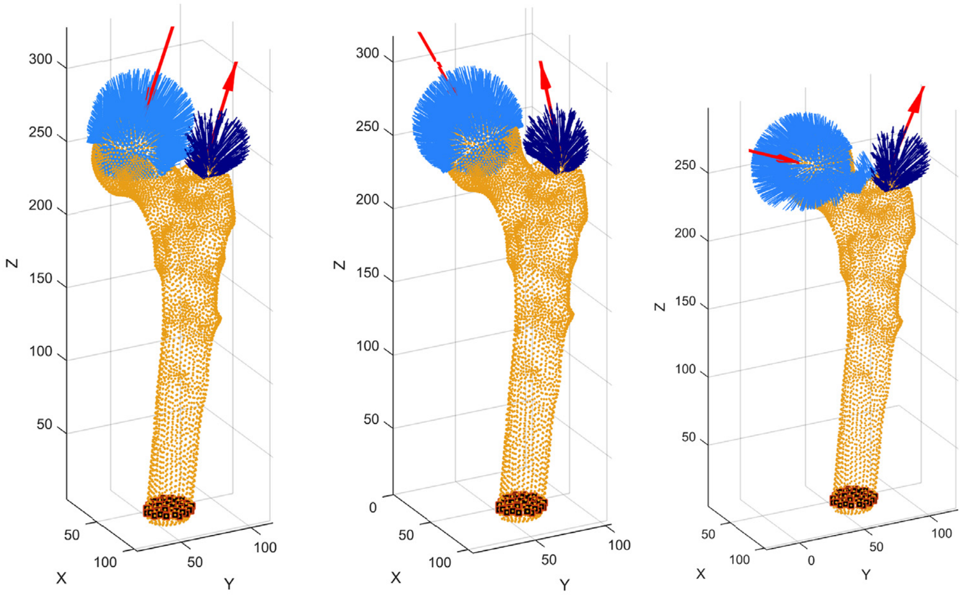

(a) Load case 1 (b) Load case 2 (c) Load case 3

Fig. 7. Loading cases adopted in the bone remodeling simulation. In order to obtain a more realistic loading distribution we combined 3 load cases simulating a standard human gait. Concentrated loads specified in Table 1 where proportionally distributed in the acetabulus and greater trochanter of the femur simulating the abductor and adductor forces on proximal femur during gait.

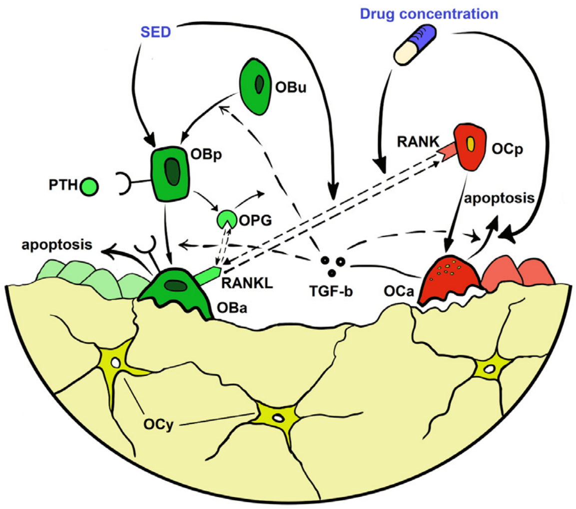

Fig. 8. Schematics of the bone cells populations model. Local strain energy density (SED) and drug concentration play a regulatory role in the dynamics of cells populations. These stimuli are not present in the original work of Lemaire et al. [21]. Artwork: Miguel T. Bahia.

action of an antiresorptive agent, drug used for the treatment and prevention of osteoporosis[1].

In the present work, the authors include both the mechanical stimuli [22] and the action of an antiresorptive agent [49], such as bisphosphonate. The drug concentration in the bone will be used here to evaluate pharmacoregulation of the bone cells population dynamics.

In mathematical terms, the temporal evolution of bone cells can be expressed by the system of ordinary differential equations shown below, Eqs. (4)–(8). The temporal changes in the cells populations occur during the bone remodeling process and are calculated over a volume of bone of sufficient size to provide consistent mean values. The variables OB_p, OB_a and OC_a refer to pre-osteoblasts, active osteoblasts and active osteoclasts, respectively. The variables BA and BM are the antiresorptive drug concentration in the bone matrix and the biomarker for bone mineral density (BMD), respectively. In this way, the following system of ordinary differential equations is described as:

$$\frac{d\mathrm{OB}_p}{dt} = D_R\pi_C + P_{\mathrm{OB}_p}\mathrm{OB}_p\Pi_\varepsilon - \frac{D_B}{\pi_C}\mathrm{OB}_p \tag{4}$$

$$\frac{d\mathrm{OB}_a}{dt} = \frac{D_B}{\pi_C}\mathrm{OB}_p - k_B\mathrm{OB}_a \tag{5}$$

$$\frac{d\mathrm{OC}_a}{dt} = D_C\pi_L - (1 + k_7\mathrm{BA})D_A\pi_C\mathrm{OC}_a \tag{6}$$

$$\frac{d\mathrm{BA}}{dt} = k_8\mathrm{BI}(1 - \mathrm{BA}) - k_9\mathrm{BA} \tag{7}$$

$$\frac{d\mathrm{BM}}{dt} = k_{10}\left(\frac{\mathrm{OB}_a}{\mathrm{OC}_a} - k_{12}\right) - k_{11}(\mathrm{BM} - 1) \tag{8}$$

where D_B is a factor of proportionality and π_C is the influence of TGF-β, expressed by:

$$D_B = f_0 d_B \pi_C = \frac{C + f_0 C^S}{C + C^S} \tag{9}$$

The RANKL influence is described by the variable π_L, and can be obtained by:

$$\pi_L = \frac{k_3}{k_4}\frac{K_L^P\pi_P\mathrm{OB}_a}{1 + \frac{k_3}{k_4} + \frac{k_1}{k_2k_0}\left(\frac{K_O^P}{\pi_P + I_0}\right)}\left(1 + \Pi_{\mathrm{BA}} + \frac{I_L + P_{RL_{\varepsilon_{\mathrm{bm}}}}}{r_L}\right) \tag{10}$$

where π_P is the fraction of occupied PTH receptors which is expressed by:

$$\pi_P = \frac{\frac{I_P}{k_P} + \frac{S_P}{k_P}}{\frac{I_P}{k_P} + \frac{k_6}{k_5}} \tag{11}$$

The symbol BI, in Eq. (7) is the concentration of anti-resorptive drug in plasma. The term $P_{RL_{\varepsilon_{\mathrm{bm}}}}$ corresponds to the variation of RANKL related to changes in the energy density of deformation, only activated in disuse or lack of loading and expressed by:

$$P_{RL_{\varepsilon_{\mathrm{bm}}}} = \kappa\left(1 - \frac{w_{\varepsilon_{\mathrm{bm}}}}{w_{\varepsilon_{\mathrm{bm_{st}}}}}\right) \tag{12}$$

where the adjustment constant κ is null for $w_{\varepsilon_{\mathrm{bm}}} \geq w_{\varepsilon_{\mathrm{bm_{st}}}}$. and positive otherwise.

The term Π_{BA} is a drug-regulatory function that simulates the effect of the external administration of an antiresorptive drug on the population of cells. The term was added in the original expression proposed by Lemaire et al. [21] for the RANKL concentration equation, being expressed by:

$$\Pi_{\mathrm{BA}} = k_{\mathrm{BA}}\mathrm{BA} \tag{13}$$

where BA is the concentration of the antiresorptive drug in the bone matrix and k_{BA} is an adjustment constant for the model.

The population of preosteoblasts OB_p increases with the differentiation of progenitor osteoblast cells with a maximal differentiation rate D_R, promoted by the growth factor TGF-β. On the other hand, the population of precursor osteoblasts decreases due to the differentiation of the precursor osteoblasts into active osteoblasts, which occurs at a maximum rate.

The mechanical stimulus is modeled adding a term in Eq. (4) by regulating the proliferation of osteoblasts as a function of the value of the locally evaluated deformation energy density [22]. The function Π_ε is the mechanoregulation and P_R is the constant indicating the proliferation of osteoblasts according to the strain energy density:

$$\Pi_\varepsilon = \Pi_{\varepsilon_{st}}\left(1 + \lambda\left(\frac{w_{\varepsilon_{\mathrm{bm}}}}{w_{\varepsilon_{\mathrm{bm_{st}}}}} - 1\right)\right) \tag{14}$$

where $\Pi_{\varepsilon_{st}}$ is the equilibrium value of Π_ε, $w_{\varepsilon_{\mathrm{bm}}}$ is the value of local strain energy density and $w_{\varepsilon_{\mathrm{bm_{st}}}}$ is the equilibrium value. Parameter λ is an adjustment constant, which is null to $w_{\varepsilon_{\mathrm{bm}}} \leq w_{\varepsilon_{\mathrm{bm_{st}}}}$ and positive otherwise.

The active osteoblast population OB_a increases according to the pre-osteoblast differentiation, which occurs with the maximum differentiation rate D_B and is inhibited by the TGF-β. Apoptosis of active osteoblasts inhibits populations growth, which occurs with apoptosis rate k_B.

Antiresorptive drugs such as bisphosphonates bind to the hydroxyapatite in the bone and inhibit its resorption by osteoclasts. In the model, the loss of efficacy of osteoclasts is simulated by a change in RANKL concentration in Eq. (10) and by an increase in

---

[1] These drugs can be divided basically into two categories: anti-resorptive agents or anabolic agents. Anti-resorptive agents reduce bone resorption, leading to increased BMD by several degrees. Estrogen, raloxifene, bisphosphonates and the human monoclonal antibody to RANKL are included in this category. On the other hand, anabolic agents such as teriparatide (PTH1-34) and total parathyroid hormone (PTH1-84), stimulate bone formation, thus increasing bone mineral density (BMD) [48].

Table 2
Parameters used in the simulation of the bone remodeling model. Values extracted from the study by Lemaire et al. [21] except $k_i (i = 7, \ldots, 12)$ and k_{BA}, which were adjusted by the authors

Symbol [unit]	Value	Description
C^s [pM]	5×10^{-3}	Number of OC to get half differentiation flux
D_A [day^{-1}]	0.7	Rate of osteoclast apoptosis caused by TGF-β
d_B [day^{-1}]	0.7	Differentiation rate of responsive osteoblasts
D_C [pM day^{-1}]	2.1×10^{-3}	Differentiation rate of osteoclast precursors
D_R [pM.day^{-1}]	7×10^{-4}	Differentiation rate of osteoblast progenitors
f_0	0.05	Fixed proportion
I_L [pM day^{-1}]	$0 - 10^6$	Rate of administration of RANKL
I_O [pM day^{-1}]	$0 - 10^6$	Rate of administration of OPG
I_P [pM day^{-1}]	$0 - 10^6$	Rate of administration of PTH
K [pM]	10	Fixed concentration of RANK
k_1 [pM^{-1} day^{-1}]	10^{-2}	Rate of OPG-RANKL binding
k_2 [day^{-1}]	10	Rate of OPG-RANKL unbinding
k_3 [pM^{-1} day^{-1}]	5.8×10^{-4}	Rate of RANK-RANKL binding
k_4 [pM day^{-1}]	1.7×10^{-2}	Rate of RANK-RANKL unbinding
k_5 [pM^{-1} day^{-1}]	0.02	Rate of PTH binding its receptor
k_6 [day^{-1}]	3	Rate of PTH unbinding
k_B [day^{-1}]	0.189	Rate of elimination of active osteoblasts
K_L^P [pmol/pmol]	3×10^6	Maximum RANKL attached to each cell surface
k_O [day^{-1}]	0.35	Rate of elimination of OPG
K_O^P [day^{-1}]	2×10^5	Minimal rate of production of OPG per cell
k_P [day^{-1}]	86	Rate of elimination of PTH
r_L [pM day^{-1}]	10^3	Rate of RANKL production and elimination
S_P [pM day^{-1}]	250	Rate of synthesis of systemic PTH
λ [adim]	1.2	Parameter of anabolic adjustment
κ [adim]	5×10^2	Parameter of RANKL inhibition
$\Pi_{\varepsilon_{st}}$ [adim]	0.5	Equilibrium of mechanoregulation function
$w_{\varepsilon_{bm_{st}}}$ [Pa]	0.78	SED inferior limit
k_7 [adim]	0.3	Hill function parameter for apoptosis of OC$_a$
k_8 [pM day^{-1}]	6×10^{-3}	Bisphosphonate transfer from plasma to bone
k_9 [1/h]	5×10^{-4}	Bisphosphonate on bone clearance rate
k_{10} [1/h]	25×10^{-5}	First order BMD rate OC$_a$/OB$_a$
k_{11} [1/h]	1.5×10^{-4}	BMD equilibrium
k_{12} [adim]	0.7979	Baseline value of OC$_a$/OB$_a$
k_{BA} [adim]	1	Parameter of the Hill function for drug regulation

the rate of apoptosis of active osteoclasts in Eq. (6). Bisphosphonate attaches to the bone in a second-order forward and first-order reverse reaction with hydroxyapatite attachment sites [49], ie, the rate of reaction is proportional to the product of two concentrations forward and only one back, respectively. The output values of Eq. (7) are within the range of [0, 1].

According to Ross et al. [49], the model uses bone mineral density (BMD) as a reference biomarker, denoting BM in Eq. (8). Considering that the term that underlies BMD is the osteoblast/osteoclast ratio, it is incorporated into the system of differential equations including a ratio between the difference of the osteoblast/osteoclast ratio and its reference value. In the absence of treatment the biomarker for BMD returns to the baseline value 1.

The model parameters are summarized in Table 2

2.4. Drucker–Prager equivalent stress

The Druker–Prager equivalent stress incorporates the hydrostatic contribution, which is suitable for the study of the bone and was adopted here. In the case of bone the failure stress under tensile loads is smaller than under compression, which is a common characteristic of brittle materials [50,51]. Although used in some previous biomechanical studies, Von Mises equivalent stress, widely employed for ductile materials, is not the most adequate. A symmetric failure criterion such as Von Mises tends both to overestimate the tensile bone strength and to underestimate the compressive bone strength. Moreover, experimental results show that a simulation with the Drucker–Praguer failure criterion predicted better the fracture location compared to the von Mises criterion [52]. Other candidate to a bone failure criterion is the Tsai–Wu quadratic criterion [53] that can account for different tensile and compressive strengths, anisotropy and interactions between strengths in different loading directions [54].

The Drucker–Prager equivalent stress is expressed by:

$$F(\sigma) = \alpha J_1 + (J_2')^{1/2} \tag{15}$$

$$J_1 = \sigma_x + \sigma_y + \sigma_z \tag{16}$$

$$J_2' = \frac{1}{2}(\sigma_x'^2 + \sigma_y'^2 + \sigma_z'^2) + \tau_{xy}^2 + \tau_{yz}^2 + \tau_{xz}^2 \tag{17}$$

where $F(\sigma)$ is the yield function, σ_x, σ_y and σ_z are the normal stresses, τ_{xy}, τ_{yz}, and τ_{xy} are the shear stresses, the symbol ($'$) indicates the deviatoric part of the stress, that is $\sigma_{ij}' = \sigma_{ij} - \delta_{ij}\sigma_m$, and $\sigma_m = \frac{1}{3}\sigma_{ii}$ is the hydrostatic stress. J_1 is the first stress invariant, J_2 is the second invariant of the deviatoric tensor, and α is a parameter related to the rate of volumetric and deviatoric deformations or dilative potential of the material, α is set to 0.07 [55]. As can be seen in Eqs. (15), (16) and (17), J_1 becomes negative when the hydrostatic stress is present, which makes the failure criterion $F(\sigma)$ smaller. Thus, the failure of an element requires a larger external loading [50].

3. Results

This section presents an FE analysis and a bone remodeling simulation developed with the proposed subject-specific FE model (Fig. 9). One loading case was implemented as illustrated in Figure 6. Results of FE analysis are showed in terms of principal stress/strains and Druker–Prager equivalent stress. Given a general

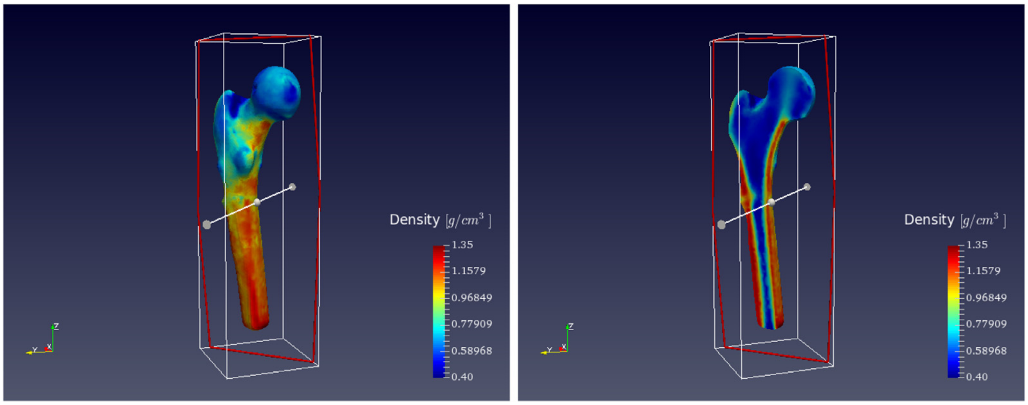

(a) Plane of section. (b) Longitudinal section

Fig. 9. Densities distribution in the reconstructed femur and longitudinal section. Visualization in Paraview 5.0 software (Sandia National Laboratory, Kitware Inc, Los Alamos National Laboratory).

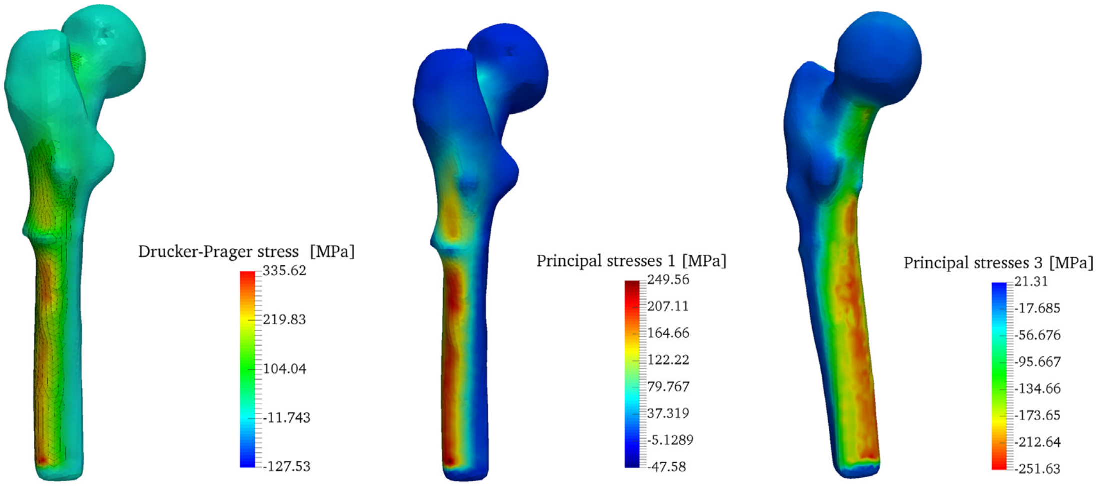

(a) Drucker-Prager stress (b) Principal stresses 1 (c) Principal stresses 3

Fig. 10. Drucker–Prager equivalent and principal stresses 1 and 3 obtained in the FE analysis of the femur with isotropic non-homogeneous elasticity modulus, boundary conditions defined in Table 1.

Table 3
Comparison between non-homogeneous and homogeneous model.

Stress and strains		Non homogeneous $E_{\text{cort}} = 10200\rho_{\text{ash}}^{2.01}$[MPa] $E_{\text{trab}} = 5307\rho_{\text{ash}} + 469$[MPa]	Homogeneous $E_{\text{cort}} = 14950$ MPa $E_{\text{trab}} = 1140$ MPa	Percentage difference
Drucker–Prager Equation stress [MPa]		334.53	328.47	2 %
Principal stress [MPa]	Max	249.53	244.11	2 %
	Min	−251.63	−253.74	1 %
Principal strains [mm/mm]	Max	0.017445	0.015561	12 %
	Min	−0.020459	−0.016860	21 %

state of stress at one point, the principal stresses correspond to the maximum normal stresses present in the planes with null shear stress components.

Results for equivalent stress and principal stresses/strains are illustrated in Figures 10 and 11. Comparing Figure 10(b) and (c) one can clearly visualize the tensile and compressive stress distribution (principal stresses 1 and 3) around the neutral axis of the femur induced by the bending moment.

The same structural analysis was performed in a femur with two homogeneous elasticity modulus distribution for cortical and trabecular bone, aiming to compare both situations: homogeneous and non-homogeneous properties. The elasticity modulus is set to 14.95 GPa for the cortical bone and 1.14 GPa for the trabecular bone, as adopted by Sotto-Maior et al. [6]. Results for both simulations are summarized in Table 3.

The behavior of both models, homogeneous and non-homogeneous, presented relatively close values for principal stress and equivalent stress. Here this result can be explained by the fact that the Young's moduli chosen for cortical and trabecular bone were close to the average values for cortical and trabecular distributions extracted from the medical images using a Gaussian mixture model[2] and applying an experimental relation.

---

[2] A probabilistic model that represents normally distributed subpopulations within an overall population.

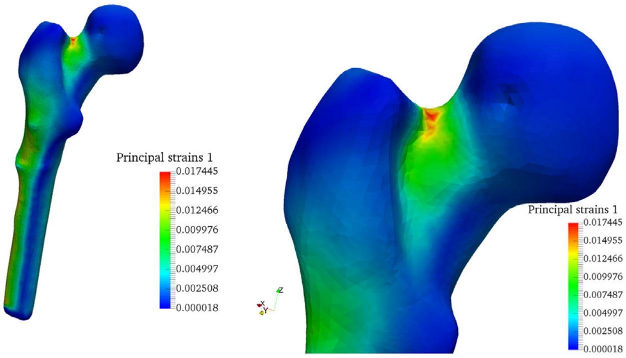

(a) Principal strains 1 (b) Zoom into the critical region

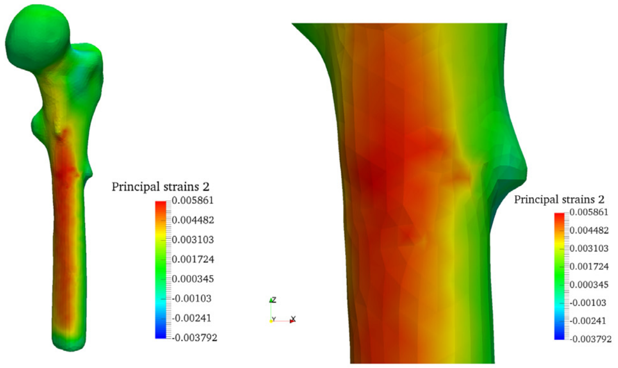

(c) Principal strains 2 (d) Zoom into the critical region

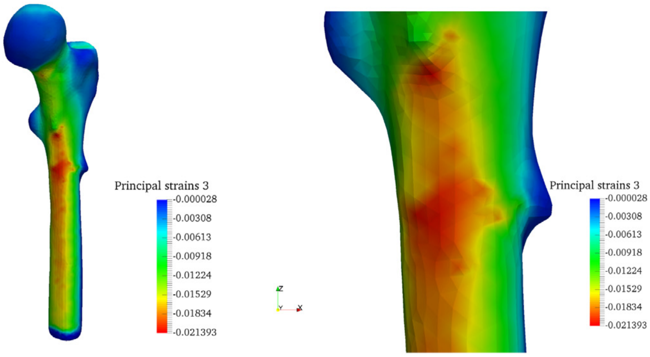

(e) Principal strains 3 (f) Zoom into the critical region

Fig. 11. Principal strains 1, 2 and 3 obtained in the FE analysis of the femur with isotropic non-homogeneous elasticity modulus, boundary conditions defined in Table 1.

It should be noted that this does not necessarily occur, so large discrepancies may occur in other simulations. On the other hand, the values of principal strains obtained for the two models were significantly different, reaching a difference of 12 and 21 % for the tensile and compressive principal strains respectively, as can be observed in Table 3. In the detail shown in Figure 11(b), it is observed that the maximum tensile principal strains are located in the upper part of the femoral neck coinciding with the typical onset of femoral fractures. In the case of principal strains 2 and 3, the maximum values are located in the diaphyseal region and close to the region where the actual fracture occurred as shown in Figure 11(d) and (f). Therefore, a failure criterion based on the principal deformations might be more successful in capturing the region achievable at femoral fracture compared to the criteria based on tension, as pointed out in previous studies [56,57].

The maximum values of Drucker–Prager equivalent stresses for both models were also close, as can be seen in Table 3. Knowledge of the extreme values for equivalent stress and the region where they appear allows the assessment of the critical regions most susceptible to fractures for this specific mechanical loading and its relative measure of magnitude compared to the neighborhood [50].

The results of the bone remodeling simulation are depicted here. The dynamics of bone cells populations model represented by Eqs. (4)–(8) is illustrated on Figure 12. The model was analyzed through numerical integration with the 4th order Runge–Kutta algorithm programmed in Matlab.

The simulation investigates the impact of adding an antiresorptive agent stimulus on the bone cells population and BMD biomarkers, as shown in Figure 12. The mechanical stimulus was set equal to a strain energy density of 0.18 Pa. The antiresorptive effect was modeled as an increase in the rate of active osteoclast apoptosis and the inclusion of a regulatory function in RANKL expression. The antiresorptive agent stimulus inclusion after the 20th day led to an increase in BMD of 3.20%.

The differentiation of pre-osteoblasts is a function of the active osteoclasts concentration. Thus, an increase in active osteoclasts apoptosis is not sufficient to produce an increase in the active osteoblasts population. Instead, it reduces the differentiation rate of the precursor osteoblasts. An increase in the osteoclast-osteoblast ratio was obtained by modifying RANKL expression with the inclusion of the drug-regulatory function, Eq. 13, into Eq. 10.

Each iteration involves three FE structural analysis (one for each loading case) and a numerical integration of the system of differential equations that governs the dynamics of cells populations and updates the material properties. The temporal evolution of the cell populations is given in cycles of 120 days. Figure 13 shows the distribution of densities in a longitudinal section of the reconstructed femur at the initial time, after 120 cycles, and final configurations after 240 cycles.

Figure 14 illustrates the cortical bone thickening in a cross section of the femur 60 mm above the inferior base, in the diaphyseal region, during the numerical simulation of the proposed bone remodeling model. One can observe an increase in the cortical bone area of approximately 7.68% compared to the initial area. This value was estimated through image segmentation using the *K*-means clustering and subsequent counting of the number of pixels in the clustered regions (adding areas 1 and 2 shown in Figure 14(d), (e) and (f). Table 4 shows average ash densities (ρ_μ), standard deviation (σ) in [g/cm^3] and percent of each bone type during iterations of the procedure for this cross section.

4. Discussion

The possibilities brought about by the use of patient-specific finite element models for the clinical practice are manifold. One can mention, for instance, the assessment of the fracture risk, the study of bone abnormalities, improved diagnosis, follow-up, among others. Thus, these models have been increasingly attracting the interest of biomechanical and medical researchers in general.

The present research addresses an interesting case study to check the model in a real-life application. Case studies of subtrochanteric region fractures are particularly interesting due to the association between low energy femoral trauma and the long-term use of bisphosphonates, a drug used worldwide in the treatment of osteoporosis [58,59].

On the other hand, according to the report of a task force of the *American Society for Bone and Mineral Research* [60], the incidence of atypical fractures is very low and it is difficult to establish a causal relationship between the use of bisphosphonates and atypical fractures, since patients are usually treated concomitantly with other drugs that suppress bone remodeling. This is an obviously controversial subject that deserves to be studied in more depth.

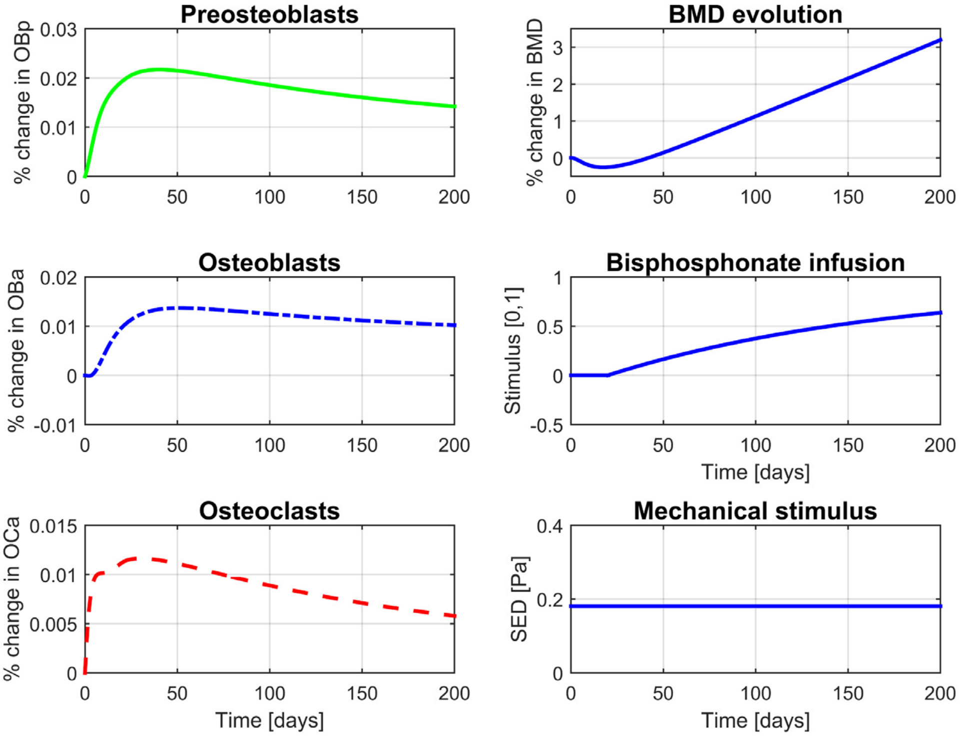

Fig. 12. Effect of mechanical stimulation on bone mineral density. Lemaire model simulation of the temporal evolution of bone populations of precursor osteoblasts (OB_p), active osteoblasts (OB_a) and active osteoclasts (OC_a). Mechanical stimulus promoted by strain energy density (SED).

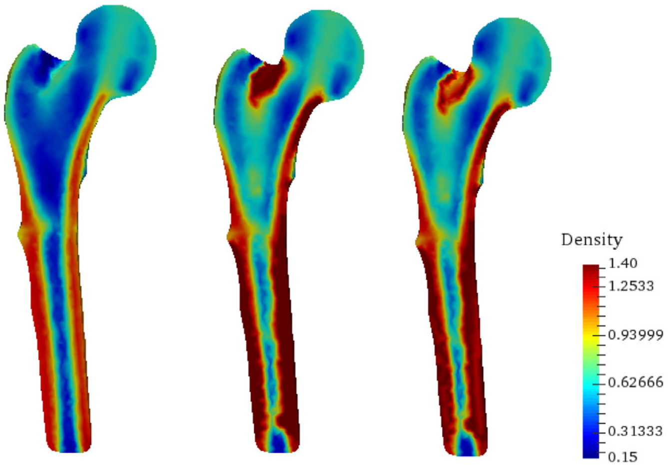

(a) Initial densities (b) Densities after 120 cycles (c) Densities after 240 cycles

Fig. 13. Densities distribution in the femur. (a), (b) and (c) show the initial configuration, after 120 and 240 cycles, respectively.

Figure 4 shows the densities distribution in the fracture region. Some discontinuities and low density areas in the direction of fracture propagation are present. The bone remodeling algorithm acted at these sites in order to recover the density. One can hypothesize that the occurrences of these discontinuities and low density areas have a strong correlation with the initiation of the fracture, and also the distribution of these areas can reveal the fracture propagation direction. However, it must be highlighted that low density or low bone mass are not the only factors contributing to the bone mechanical strength and thus, an increased fracture risk. In this sense, the bone quality involves other aspects that would be determinant to define the mechanical strength, such as bone geometry (shape and size of bone), micro-architecture, collagen maturity, microdamage accumulation, rate of bone turnover and properties of the mineral, such as its distribution, composition, orientation, among others [61]. In the case of atypical femur fractures, there is still a clear lack of understanding regarding its mechanisms of action [62]. These kind of fractures differ from traumatic or stress fractures in aspects such as location, angle of progression across the cortex and level of physical activity of the patient. It is also reported the emergence of a small callus of rapid bone formation attempting to stabilize the periosteum in the femur [59].

The medical images available for this research presented severe limitations in resolution, what required different strategies to obtain a better segmentation. Parts of the femur with well defined contour and a more pronounced cortical thickness are easily segmented, even with common histogram-based thresholds methods. However, regions of low density and greater presence of trabecular bone require a more sophisticated procedure. In this study we adopted a two-step segmentation with the K-means clustering algorithm as initial segmentation prior to the application of iterated conditional mode (ICM) algorithm, producing satisfactory results. We have performed contour smoothing by applying sequential morphological operations. In this sense, Matlab's Image Processing Toolbox offers useful built-in functions, which seems to be quite effective in this study.

The behavior of inhomogeneous isotropic material model was compared to the homogeneous one performing two FE simulations. In this study, it was not possible to observe significant differences between both models regarding principal stress and strains and Drucker–Prager equivalent stress. Note that the Young's modulus values chosen for cortical and trabecular bone in the homogeneous model were very close to the average values mapped in the CT images, verified using a Gaussian mixture model. Considering that this is not always the case, it would be hasty to conclude that the heterogeneous model produces the same results. The models were significantly different in terms of principal strains: 12 and 21 % for

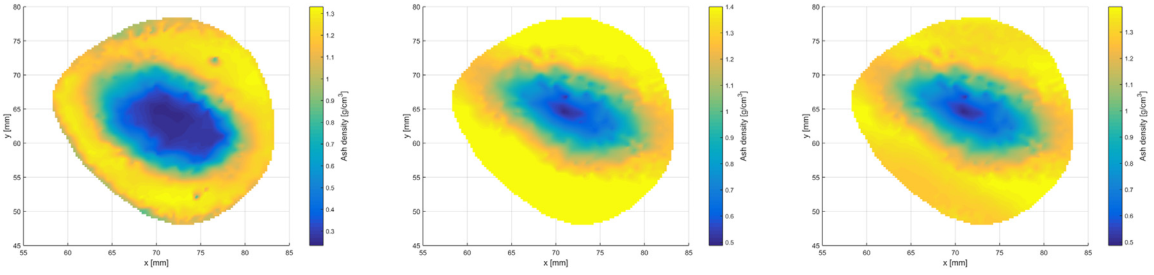

(a) Initial densities (b) Densities 120 cycles (c) Densities 240 cycles

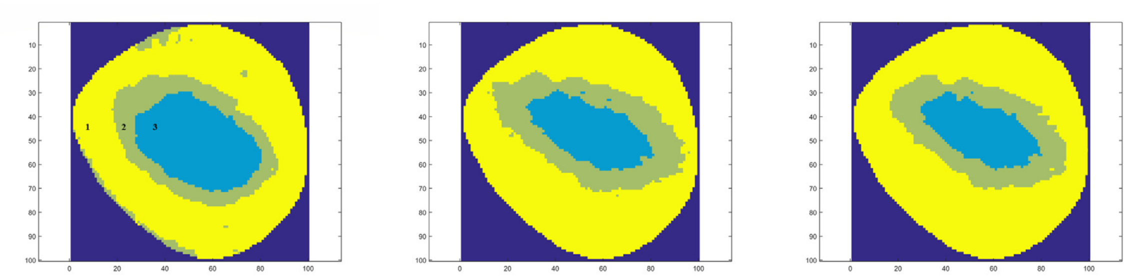

(d) K-means clustering initial (e) K-means clustering 120 cycles (f) K-means clustering 240 cycles

Fig. 14. Cross section of the femur in the diaphyseal region 60 mm above the femur lower end: (a), (b) and (c) are initial densities distribution, after 120 cycles and 240 cycles, respectively; (d), (e) and (f) correspond to the segmentation of the cortical region (adding areas 1 and 2) at initial time, after 120 cycles and 240 cycles, respectively. Image segmentation using K-means clustering algorithm was adopted to evaluate the percent increase of the cortical region.

Table 4
Average ash density (ρ_μ), standard deviation (σ) in [g/cm^3] and percentage of each bone type during procedure iterations for the transversal section of the femur illustrated in Figure 14.

Bone type	Initial configuration		120 cycles		240 cycles	
	Percentage	$\rho_\mu \pm \sigma$[g/cm^3]	Percentage	$\rho_\mu \pm \sigma$[g/cm^3]	Percentage	$\rho_\mu \pm \sigma$[g/cm^3]
Trabecular	20.84%	0.365 ± 0.105	14.46%	0.539 ± 0.034	13.14%	0.537 ± 0.034
Cortical	79.16%	1.139 ± 0.165	85.54%	1.281 ± 0.184	86.86%	1.247 ± 0.168

the maximum values of tensile and compressive strains, respectively. In addition to that, the maximum values of tensile strains were observed at the femoral neck, which is the most common region of fractures events. For the main deformations 2 and 3, the maximum values were located at the diaphyseal region, close to the actual femur fracture. Assuming that the crack growth depends on the directions of the principal strains, this result corroborates studies such as Poelert et al. [14], that pointed out that bone fracture is driven by strains, and also that strain-based failure criteria are more successful in capturing the onset of the fracture as compared to stress-based criteria [56,57]. Thus, the patient specific FE analysis method can be adopted as a reliable auxiliary tool in the prediction of fractures. Better accuracy will require higher quality medical images and some additional evaluations in the finite element mesh. The use of error estimators, a mesh quality metrics, a convergence study, and the adoption of a quadratic element constitute good practices in this regard. Considering that the method is not fully automated and requires significant user intervention, further studies are required before its adoption in the clinical practice.

Particularly in this simulation, the authors dealt with images with low bit depth and the refinement of finite elements followed some software constraints regarding maximum matrix size. Given this context, it is reasonable to argue that, in special case studies, FE model needs to incorporate the patient's individual characteristics to obtain more accurate results.

A structural analysis in the context of biomechanics involves some simplifications. One of them refers to the Newmann and Dirichlet boundary conditions adopted in the simulation. Despite being based on biomechanical studies, these will always be a simplified version of the complex real physiological loading conditions, which are cyclic, presents dynamic joint forces and involves the participation of muscles and tendons that can hardly be fully recovered in the simulation. A possible way of assessing the effects of real boundary conditions is to simulate different loading cases aiming to cover a larger range of daily activities scenarios. Another option would be to feed the boundary conditions with the output data of an inverse-dynamic analysis in conjunction with a musculoskeletal model [63].

For the structural analysis, there are other alternatives to FEM. Mesh-free methods, for instance, whose field functions are approximated within a domain of influence rather than an element, is an option to be considered. The mesh independence results in accuracy, smoothness of the stress fields and advantages when handling domains of very complex geometry in comparison with classical mesh discretization techniques. This allows dealing with large distortions of soft materials and to explicitly simulate fluids flow [64–66]. The definition of influence-domains varies according to the family of mesh-free method. A non exhaustive list includes: element free Galerkin, local Petrov–Galerkin, moving least squares, radial basis function, and fixed-grid methods, such as Cartesian grid and the Extended Finite Element Method (XFEM) [67–71].

Regarding the choice of material model as linear elastic with transient variation of Young modulus, it seems a suitable option, since for mechanical loadings within the range of physiological conditions the bone behaves as linearly elastic [72]. The experimental relations between Young modulus and bone ash density available in the literature have shown good agreement with experimental data. However, there are still a few works evaluating the effectiveness of these relations in bone disease scenarios, such as osteoporosis or osteopenia.

An interesting aspect in the development of this work is the fact that all computational codes were written in Matlab. Apart from Paraview and Meshlab softwares used in visualization and generation of surface file data (STL file), the authors did not use any others specialized commercial programs such as medical image editors and finite elements platforms. This choice seems challenging at first, but on the other hand, it provided greater versatility and insight into the search for solutions by numerical methods.

The simulation of the bone remodeling model including the effect of an antiresorptive drug was able to replicate both the overall increase in bone ash density and the thickening of the cortical bone, which are clinically expected outcomes in an osteoporosis treatment. The model allows the variation of the drug concentration by providing different local remodeling responses. However, a comparison of the results with actual clinical data is required in order to assess its predictive capacity and its limitations. Here, we sought to incorporate elements of the bone's biological behavior into the model seeking to produce plausible clinical observations. The model presents potential for use as a predictive tool in clinical routine, but further studies should be developed to fit the model with real clinical data. Future works must move in this direction.

Other perspective for the continuity of this study is the incorporation of a crack growth model in order to try to reproduce the propagation of the actual femur fracture. A theoretical background in this sense can be given by the energy minimal crack growth and phase-field methods, that allows the determination of both the direction and the onset of the crack growth [73].

5. Conclusion

This study describes a complete process of building a subject-specific FE model that was applied to a femur with an atypical fracture. The results obtained in 3D reconstruction were considered satisfactory despite the limitations in resolution of the images. Then, a FE analysis and a bone remodeling simulation were carried out using a model based on dynamics of cells populations. Principal stress and equivalent stress for inhomogeneous and homogeneous material models obtained in the FE analysis reveals no significant differences for the chosen values. Regarding principal strains, these differences were significant and the maximum values appeared relatively close to both the typical femoral fracture region (tensile principal strain) and the diaphyseal region near the actual fracture (principal strains 2 and 3). These results, therefore, indicate that a strain-based failure criterion can be more effective in the prediction of the onset of fracture than a stress-based criterion.

The authors conclude that in ordinary simulations, the adoption of standard Young modulus for cortical and trabecular bone, although unrealistic, can offer satisfactory results since the chosen values are close to the real ones. This was reproduced in the present study. We stress that subject-specific FE models must be the first choice considering special clinical cases, assessment of fracture risk or stress/strains levels. Because the method requires a high level of human intervention and expertise, further efforts are necessary before its adoption into clinical practice. Furthermore, the bone remodeling model incorporating a pharmacological regulation produced encouraging results in terms of bone adaptive behavior reproduction. Future works must explore the pharmacological regulation in different scenarios of dosing regimens.

Disclosure statement

There is not conflict of interest to declare.

Funding

None

Ethical approval

The medical images used in this study were handled according to institutional policies and procedures. The donor of the CT images signed an informed consent to collection and use of data for research purposes.

Acknowledgments

The authors would like to acknowledge Dr. Marcelo de Medeiros Pinheiro of the Department of Medicine of the Universidade Federal de São Paulo (UNIFESP) for providing the CT image data used in this study. Thanks also go to Prof. Monica Campiteli of Instituto de Física de São Carlos of the Universidade de São Paulo for the suggestions and revision of the manuscript.

Supplementary material

Supplementary material associated with this article can be found, in the online version, at doi:10.1016/j.medengphy.2019.05.005.

References

[1] Pinheiro MdM. Mortalidade após fratura por osteoporose. Arq Bras Endocrinol Metabol 2008;52(7):1071–2.

[2] Pinheiro MdM, Eis SR. Epidemiology of osteoporotic fractures in brazil: what we have and what we need. Arq Bras Endocrinol Metabol 2010;54(2):164–70.

[3] Fortes ÉM, Raffaelli MP, Bracco OL, Takata ET, Reis FB, Santili C, et al. High morbid-mortability and reduced level of osteoporosis diagnosis among elderly people who had hip fractures in São Paulo city. Arq Bras Endocrinol Metabol 2008;52(7):1106–14.

[4] Bayraktar HH, Morgan EF, Niebur GL, Morris GE, Wong EK, Keaveny TM. Comparison of the elastic and yield properties of human femoral trabecular and cortical bone tissue. J Biomech 2004;37(1):27–35.

[5] Trabelsi N, Milgrom C, Yosibash Z. Patient-specific fe analyses of metatarsal bones with inhomogeneous isotropic material properties. J Mech Behav Biomed Mater 2014;29:177–89.

[6] Sotto-Maior BS, Mercuri EGF, Senna PM, Assis NMSP, Francischone CE, Del Bel Cury AA. Evaluation of bone remodeling around single dental implants of different lengths: a mechanobiological numerical simulation and validation using clinical data. Comput Methods Biomech Biomed Eng 2016;19(7):699–706.

[7] Doblaré M, Garcıa J. Anisotropic bone remodelling model based on a continuum damage-repair theory. J Biomech 2002;35(1):1–17.

[8] Morgan EF, Bayraktar HH, Keaveny TM. Trabecular bone modulus–density relationships depend on anatomic site. J Biomech 2003;36(7):897–904.

[9] Barkaoui A, Kahla RB, Merzouki T, Hambli R. Age and gender effects on bone mass density variation: finite elements simulation. Biomech Model Mechanobiol 2016:1–15.

[10] Schileo E, Taddei F, Malandrino A, Cristofolini L, Viceconti M. Subject-specific finite element models can accurately predict strain levels in long bones. J Biomech 2007;40(13):2982–9.

[11] Schileo E, DallfiAra E, Taddei F, Malandrino A, Schotkamp T, Baleani M, et al. An accurate estimation of bone density improves the accuracy of subject-specific finite element models. J Biomech 2008a;41(11):2483–91.

[12] Viceconti M, Davinelli M, Taddei F, Cappello A. Automatic generation of accurate subject-specific bone finite element models to be used in clinical studies. J Biomech 2004;37(10):1597–605.

[13] Trabelsi N, Yosibash Z, Milgrom C. Validation of subject-specific automated p-fe analysis of the proximal femur. J Biomech 2009;42(3):234–41.

[14] Poelert S, Valstar E, Weinans H, Zadpoor AA. Patient-specific finite element modeling of bones. Proc Inst Mech Eng H: J Eng Med 2013;227(4):464–78.

[15] Crawford RP, Cann CE, Keaveny TM. Finite element models predict in vitro vertebral body compressive strength better than quantitative computed tomography. Bone 2003;33(4):744–50.

[16] Harrigan TP, Jasty M, Mann RW, Harris WH. Limitations of the continuum assumption in cancellous bone. J Biomech 1988;21(4):269–75.

[17] Pardo XM, Carreira MJ, Mosquera A, Cabello D. A snake for ct image segmentation integrating region and edge information. Image Vis Comput 2001;19(7):461–75.

[18] Truc PT, Kim T-S, Lee S, Lee Y-K. A study on the feasibility of active contours on automatic ct bone segmentation. J Dig Imaging 2010;23(6):793–805.

[19] Taddei F, Cristofolini L, Martelli S, Gill H, Viceconti M. Subject-specific finite element models of long bones: an in vitro evaluation of the overall accuracy. J Biomech 2006;39(13):2457–67.
[20] Demirkaya O, Asyali MH, Sahoo PK. Image processing with MATLAB: applications in medicine and biology. CRC Press; 2008.
[21] Lemaire V, Tobin FL, Greller LD, Cho CR, Suva LJ. Modeling the interactions between osteoblast and osteoclast activities in bone remodeling. J Theor Biol 2004;229(3):293–309.
[22] Scheiner S, Pivonka P, Hellmich C. Coupling systems biology with multiscale mechanics, for computer simulations of bone remodeling. Comput Methods Appl Mech Eng 2013;254:181–96.
[23] Müller ME, Nazarian S, Koch P, Schatzker J. The comprehensive classification of fractures of long bones. Springer Science & Business Media; 2012.
[24] Seinsheimer F. Subtrochanteric fractures of the femur. J Bone Joint Surg Am 1978;60(3):300–6.
[25] James LG. Fractures of hip, acetabulum, and pelvis. Campbell's Oper orthop 1998:2181–279.
[26] Meijster A. Efficient sequential and parallel algorithms for morphological image processing. University Library Groningen; 2004.
[27] Reyes-Aldasoro CC. Biomedical image analysis recipes in MATLAB: for life scientists and engineers. John Wiley & Sons; 2015.
[28] Bovik AC. The essential guide to image processing. Academic Press; 2009.
[29] Gonzalez RC, Woods RE. Digital image processing. Upper Saddle River, NJ: Prentice Hall; 2012.
[30] Cignoni P, Callieri M, Corsini M, Dellepiane M, Ganovelli F, Ranzuglia G. MeshLab: an Open-Source Mesh Processing Tool. In: Scarano V, Chiara RD, Erra U, editors. Proceedings of the Eurographics Italian chapter conference. The Eurographics Association; 2008. ISBN 978-3-905673-68-5. doi: 10.2312/LocalChapterEvents/ItalChap/ItalianChapConf2008/129-136.
[31] Kazhdan M, Hoppe H. Screened poisson surface reconstruction. ACM Trans Graph (ToG) 2013;32(3):29.
[32] Zannoni C, Mantovani R, Viceconti M. Material properties assignment to finite element models of bone structures: a new method. Med Eng Phys 1999;20(10):735–40.
[33] Schroeder WJ, Avila LS, Hoffman W. Visualizing with VTK: a tutorial. IEEE Comput Graph Appl 2000;20(5):20–7.
[34] Dragomir-Daescu D, Salas C, Uthamaraj S, Rossman T. Quantitative computed tomography-based finite element analysis predictions of femoral strength and stiffness depend on computed tomography settings. J Biomech 2015;48(1):153–61.
[35] Carter DR, Hayes WC. The compressive behavior of bone as a two-phase porous structure. J Bone Jt Surg 1977;59(7):954–62.
[36] Snyder SM, Schneider E. Estimation of mechanical properties of cortical bone by computed tomography. J Orthop Res 1991;9(3):422–31.
[37] Kaneko TS, Bell JS, Pejcic MR, Tehranzadeh J, Keyak JH. Mechanical properties, density and quantitative ct scan data of trabecular bone with and without metastases. J Biomech 2004;37(4):523–30.
[38] Keller TS. Predicting the compressive mechanical behavior of bone. J Biomech 1994;27(9):1159–68.
[39] Helgason B, Perilli E, Schileo E, Taddei F, Brynjólfsson S, Viceconti M. Mathematical relationships between bone density and mechanical properties: a literature review. Clin Biomech 2008;23(2):135–46.
[40] Yosibash Z, Trabelsi N, Milgrom C. Reliable simulations of the human proximal femur by high-order finite element analysis validated by experimental observations. J Biomech 2007;40(16):3688–99.
[41] Nedoma J, Stehlik J. Mathematical and computational methods and algorithms in biomechanics: human skeletal systems, 12. John Wiley & Sons; 2011.
[42] Firoozbakhsh K, Cowin S. An analytical model of Pauwels' functional adaptation mechanism in bone. J Biomech Eng 1981;103(4):246–52.
[43] Speirs AD, Heller MO, Duda GN, Taylor WR. Physiologically based boundary conditions in finite element modelling. J Biomech 2007;40(10):2318–23.
[44] Hambli R, Boughattas MH, Daniel J-L, Kourta A. Prediction of denosumab effects on bone remodeling: a combined pharmacokinetics and finite element modeling. J Mech Behav Biomed Mater 2016;60:492–504.
[45] Carter D, Fyhrie DP, Whalen R. Trabecular bone density and loading history: regulation of connective tissue biology by mechanical energy. J Biomech 1987;20(8):785789–7794.
[46] Burr DB, Allen MR. Basic and applied bone biology. Academic Press; 2013.
[47] Mercuri E, Daniel A, Hecke M, Carvalho L. Influence of different mechanical stimuli in a multi-scale mechanobiological isotropic model for bone remodelling. Med Eng Phys 2016;38(9):904–10.
[48] Szulc P, Bouxsein ML. Overview of osteoporosis: Epidemiology and clinical management. Verteb Fract Initiat Resour Doc I 2011.
[49] Ross DS, Mehta K, Cabal A. Mathematical model of bone remodeling captures the antiresorptive and anabolic actions of various therapies. Bull Math Biol 2017;79(1):117–42.
[50] Bessho M, Ohnishi I, Matsuyama J, Matsumoto T, Imai K, Nakamura K. Prediction of strength and strain of the proximal femur by a CT-based finite element method. J Biomech 2007;40(8):1745–53.
[51] Cordey J, Gautier E. Strain gauges used in the mechanical testing of bones part i: theoretical and technical aspects. Injury 1999;30:SA7–SA13.
[52] Derikx LC, Vis R, Meinders T, Verdonschot N, Tanck E. Implementation of asymmetric yielding in case-specific finite element models improves the prediction of femoral fractures. Comput Methods Biomech Biomed Eng 2011;14(02):183–93.
[53] Tsai SW, Wu EM. A general theory of strength for anisotropic materials. J Compos Mater 1971;5(1):58–80.
[54] Keaveny T, Wachtel E, Zadesky S, Arramon Y. Application of the Tsai–Wu quadratic multiaxial failure criterion to bovine trabecular bone. J Biomech Eng 1999;121(1):99–107.
[55] Kupfer H, Hilsdorf HK, Rusch H. Behavior of concrete under biaxial stresses. J. Proc. 1969;66:656–66.
[56] Schileo E, Taddei F, Cristofolini L, Viceconti M. Subject-specific finite element models implementing a maximum principal strain criterion are able to estimate failure risk and fracture location on human femurs tested in vitro. J Biomech 2008b;41(2):356–67.
[57] Nalla RK, Kinney JH, Ritchie RO. Mechanistic fracture criteria for the failure of human cortical bone. Nat Mater 2003;2(3):164.
[58] Odvina CV, Zerwekh JE, Rao DS, Maalouf N, Gottschalk FA, Pak CY. Severely suppressed bone turnover: a potential complication of alendronate therapy. J Clin Endocrinol Metabol 2005;90(3):1294–301.
[59] Geissler JR, Bajaj D, Fritton JC. American society of biomechanics journal of biomechanics award 2013: cortical bone tissue mechanical quality and biological mechanisms possibly underlying atypical fractures. J Biomech 2015;48(6):883–94.
[60] Shane E, Burr D, Ebeling PR, Abrahamsen B, Adler RA, Brown TD, et al. Atypical subtrochanteric and diaphyseal femoral fractures: report of a task force of the american society for bone and mineral research. J Bon Miner Res 2010;25(11):2267–94.
[61] van der Meulen MC, Boskey AL. Atypical subtrochanteric femoral shaft fractures: role for mechanics and bone quality. Arthr Res Therapy 2012;14(4):220.
[62] Shane E, Burr D, Abrahamsen B, Adler RA, Brown TD, Cheung AM, et al. Atypical subtrochanteric and diaphyseal femoral fractures: second report of a task force of the american society for bone and mineral research. J Bone Miner Res 2014;29(1):1–23.
[63] Seo J-W, Kang D-W, Kim J-Y, Yang S-T, Kim D-H, Choi J-S, et al. Finite element analysis of the femur during stance phase of gait based on musculoskeletal model simulation. Bio-med Mater Eng 2014;24(6):2485–93.
[64] Belinha J. Meshless methods in biomechanics. Springer; 2014.
[65] Doweidar M, Calvo B, Alfaro I, Groenenboom P, Doblaré M. A comparison of implicit and explicit natural element methods in large strains problems: Application to soft biological tissues modeling. Comput Methods Appl Mech Eng 2010;199(25–28):1691–700.
[66] Wong KC, Wang L, Zhang H, Liu H, Shi P. Meshfree implementation of individualized active cardiac dynamics. Comput Med Imaging Graph 2010;34(1):91–103.
[67] Doblare M, Cueto E, Calvo B, Martinez M, Garcia J, Cegonino J. On the employ of meshless methods in biomechanics. Comput Methods Appl Mech Eng 2005;194(6–8):801–21.
[68] Fasshauer GE. Meshfree approximation methods with MATLAB, 6. World Scientific; 2007.
[69] Babuška I, Melenk JM. The partition of unity method. Int J Numer Methods Eng 1997;40(4):727–58.
[70] Belytschko T, Parimi C, Moës N, Sukumar N, Usui S. Structured extended finite element methods for solids defined by implicit surfaces. Int J Numer Methods Eng 2003;56(4):609–35.
[71] Sukumar N, Prévost J-H. Modeling quasi-static crack growth with the extended finite element method part i: Computer implementation. Int J Solids Struct 2003;40(26):7513–37.
[72] Juszczyk MM, Cristofolini L, Viceconti M. The human proximal femur behaves linearly elastic up to failure under physiological loading conditions. J Biomech 2011;44(12):2259–66.
[73] Sutula D, Kerfriden P, van Dam T, Bordas SP. Minimum energy multiple crack propagation. part I: theory and state of the art review. Eng Fract Mech 2018;191:205–24.